This is a repository copy of *Considerations on a phase-field model for adhesive fracture*.

White Rose Research Online URL for this paper:
https://eprints.whiterose.ac.uk/159647/

Version: Accepted Version

Article:
Ghaffari Motlagh, Y. and de Borst, R. orcid.org/0000-0002-3457-3574 (2020) Considerations on a phase-field model for adhesive fracture. International Journal for Numerical Methods in Engineering, 121 (13). pp. 2946-2963. ISSN 0029-5981

https://doi.org/10.1002/nme.6341

This is the peer reviewed version of the following article: Ghaffari Motlagh, Y, de Borst, R. Considerations on a phase-field model for adhesive fracture. Int J Numer Methods Eng. 2020; 121: 2946– 2963 which has been published in final form at https://doi.org/10.1002/nme.6341. This article may be used for non-commercial purposes in accordance with Wiley Terms and Conditions for Use of Self-Archived Versions. This article may not be enhanced, enriched or otherwise transformed into a derivative work, without express permission from Wiley or by statutory rights under applicable legislation. Copyright notices must not be removed, obscured or modified. The article must be linked to Wiley's version of record on Wiley Online Library and any embedding, framing or otherwise making available the article or pages thereof by third parties from platforms, services and websites other than Wiley Online Library must be prohibited.

Reuse
Items deposited in White Rose Research Online are protected by copyright, with all rights reserved unless indicated otherwise. They may be downloaded and/or printed for private study, or other acts as permitted by national copyright laws. The publisher or other rights holders may allow further reproduction and re-use of the full text version. This is indicated by the licence information on the White Rose Research Online record for the item.

Takedown
If you consider content in White Rose Research Online to be in breach of UK law, please notify us by emailing eprints@whiterose.ac.uk including the URL of the record and the reason for the withdrawal request.

eprints@whiterose.ac.uk
https://eprints.whiterose.ac.uk/

Received: Added at production | Revised: Added at production | Accepted: Added at production

DOI: xxx/xxxx

ARTICLE TYPE

Considerations on a phase-field model for adhesive fracture

Yousef Ghaffari Motlagh | René de Borst*

Department of Civil and Structural Engineering, University of Sheffield, Sheffield, S1 3JD, UK

Correspondence
*René de Borst, Department of Civil and Structural Engineering, University of Sheffield, Sheffield S1 3JD, UK. Email: r.deborst@sheffield.ac.uk

Summary

A recently proposed phase-field model for cohesive fracture [1] is examined. Previous investigations have shown stress oscillations to occur when using unstructured meshes. It is now shown that the use of Non-Uniform Rational B-Splines (NURBS) as basis functions rather than traditional Lagrange polynomials significantly reduces this oscillatory behaviour. Moreover, there is no effect on the global structural behaviour, as evidenced through load-displacement curves. The phase-field model imposes restrictions on the interpolation order of the NURBS used for the three different fields: displacement, phase field, and crack opening. This holds within the Bézier element, but also at the boundaries, where a reduction to C^0-continuity yields optimal results. Application to a range of cases, including debonding of a hard fibre embedded in a soft matrix, illustrates the potential of the cohesive phase-field model.

KEYWORDS:
Phase-field models, cracking, isogeometric analysis, cohesive fracture, adhesive fracture

1 | INTRODUCTION

Numerical approaches to the modelling of fracture initiation and propagation can be divided in two main categories, namely discrete crack models and smeared crack models. In discrete crack models, the discontinuities are introduced into the displacement field using interface elements which are inserted in the mesh a priori [2,3,4,5], by means of remeshing [6,7,8], or by enriching the basis by inserting discontinuities [9,10]. These methods have been investigated widely and successful applications have been reported. However, robust extensions to complex three-dimensional problems have shown to be non-trivial.

Smeared approaches are an alternative, in which the sharp discontinuity is distributed over a small, but finite width [11]. Early smeared approaches appeared to be deficient in the sense that they caused a loss of well-posedness of the boundary value problem at, or close to structural failure. The concomitant grid sensitivity then prevents physically meaningful answers. A host of solutions have been proposed as a remedy, but gradient-enhanced damage models appear to be particularly effective and powerful to model fracture in quasi-brittle and ductile materials [12].

More recently, the variational approach has become popular as an elegant and mathematically well-founded approach to brittle fracture [13]. In it, the solution to the fracture problem is found as the minimiser of a global energy functional. A phase-field implementation of this model has been proposed by Bourdin *et al.* [14] and has been cast in a damage-like, engineering format by Miehe *et al.* [15,16]. Indeed, the phase-field approach to brittle fracture can be classified as a smeared approach, and bears much similarity to gradient-enhanced damage models [17].

Cohesive-zone models have become increasingly popular for predicting crack propagation in quasi-brittle and ductile materials [18,19,20,21]. Different from Linear Elastic Fracture Mechanics the crack opening is a crucial element in the constitutive formulation. Typically, the crack opening is not available in the aforementioned phase-field approach to brittle fracture.

A phase-field model, in which an auxiliary field was introduced for explicitly modelling the crack opening, was therefore introduced to model cohesive fracture[1,22,23]. With the phase field also as an independent variable this results in a three-field approach. To avoid using an auxiliary field, level set methods have also been utilised[24,25]. Other approaches, which set out to model cohesive fracture rather exploit the variational phase-field approach to brittle fracture and attempt to obtain a cohesive-like fracture behaviour by modifying the assumed phase-field distribution perpendicular to the centre of the crack, the degradation function[26,27,28,29,30], or attempt to reconstruct the crack opening from the phase field[31,32].

The cohesive phase-field model with an independent interpolation of the crack opening[1] is an elegant and, in principle, a very powerful way to implement cohesive fracture within the context of phase-field modelling. However, subsequent investigations revealed some issues, such as a difficulty to drive a cohesive crack in an arbitrary direction, i.e. not along a pre-defined crack[22], and stress oscillations for unstructured meshes[23]. The first issue is likely to be a deficiency of the current formulation. Indeed, the current formulation for cohesive fracture does not result in set of partial differential equations which completely determines the evolution of the cracks, as there are ad hoc rules needed to determine crack nucleation, propagation, or bifurcation, which is in contrast to the phase-field formulations for brittle fracture. Herein, we address the second issue, namely the emergence of stress oscillations for unstructured meshes. It has been hypothesised before that the fact the interpolations for the displacements yield an interpolation for the stresses which do not match that of the the cohesive tractions which derive from the interpolation of the displacement jump (which is forced to be constant normal to the crack) can be responsible for this behaviour[23].

Herein, we improve the accuracy by reverting from a standard Lagrangian interpolation[1] to a Bernstein-Bézier discretisation. Non-Uniform Rational B-Splines (NURBS) are used as in standard IsoGeometric Analysis, except that the basis functions are now not C^{p-1} continuous across element boundaries. We exploit this lower order to improve the modelling of the displacement jump at the crack, since interpolations which are C^0-continuous at element boundaries yield better results. To this end the sensitivity of the results with respect to the orders of the discretisation and the element continuity of the three fields have investigated. We furthermore examine the performance of the present phase-field model when considering interfaces between materials with significantly different stiffnesses.

In Section 2 we succinctly summarise the phase-field model for cohesive fracture, followed by the discretisation in Section 3 for sake of completeness. Some of the fundamental issues are examined next for a one-dimensional bar subject to tension. More challenging two-dimensional cases are investigated in Section 5, including the loss of adhesion between a stiff fibre and its surrounding matrix.

2 | PHASE-FIELD MODEL FOR COHESIVE FRACTURE

We consider a volume Ω with an internal discontinuity boundary Γ. The position of a material point is determined by the coordinate $\boldsymbol{x}$ in a Cartesian reference frame. Displacement and traction components are prescribed along disjoint parts of the external boundary of the domain, $\partial\Omega_{g_i}$ and $\partial\Omega_{h_i}$, respectively.

2.1 | Cohesive fracture

The essential difference between brittle and cohesive fracture models is the dependence of the fracture energy on the crack opening for the latter type of models. While in the former class of models the fracture energy $\mathcal{G}_c$ is instantly dissipated upon the creation of a unit crack surface, the energy is released gradually in cohesive-zone models, as the energy dissipation is governed by a fracture energy function:

$$\mathcal{G} = \mathcal{G}\Big(\llbracket \boldsymbol{u} \rrbracket, \kappa\Big) \tag{1}$$

which depends on the jump of the displacement field $\llbracket \boldsymbol{u} \rrbracket$ across the discontinuity Γ and on a history parameter κ. The cohesive tractions are obtained through differentiation of the fracture energy with respect to the crack opening:

$$\boldsymbol{t}\Big(\llbracket \boldsymbol{u} \rrbracket, \kappa\Big) = \frac{\partial \mathcal{G}}{\partial \llbracket \boldsymbol{u} \rrbracket} \tag{2}$$

As starting point for the derivation of the phase-field approximation to cohesive fracture, we first consider the total potential energy in the sense of Griffith's theory for brittle fracture[13]:

$$\Psi_{pot} = \int_{\Omega} \psi_e(\boldsymbol{\varepsilon}) \mathrm{d}V + \int_{\Gamma} \mathcal{G}_c \mathrm{d}A \tag{3}$$

We assume small strain deformations, and define the infinitesimal strain tensor, $\boldsymbol{\varepsilon}$, with components

$$\varepsilon_{ij} = u_{(i,j)} = \frac{1}{2}\left(\frac{\partial u_i}{\partial x_j} + \frac{\partial u_j}{\partial x_i}\right) \tag{4}$$

as the deformation measure. We assume isotropic linear elasticity, such that the elastic energy density is given by

$$\psi_e = \frac{1}{2}\lambda\varepsilon_{ii}\varepsilon_{jj} + \mu\varepsilon_{ij}\varepsilon_{ij} \tag{5}$$

with λ and μ the Lamé constants and using the Einstein convention. In Equation (3), the fracture energy is denoted by $\mathcal{G}_c$. An irreversibility condition is included which enforces that cracks can only nucleate and propagate, and not heal [14], but we note that not all forms of an irreversibility condition may be appropriate [33]. Similar to brittle fracture, but now using the fracture energy function (1), the potential energy for cohesive fracture reads:

$$\Psi_{pot} = \int_\Omega \psi_e(\boldsymbol{\varepsilon})\mathrm{d}V + \int_\Gamma \mathcal{G}\Big(\llbracket \boldsymbol{u} \rrbracket, \kappa\Big)\mathrm{d}A \tag{6}$$

2.2 | Phase-field formulation and boundary conditions

The variational approach to brittle fracture [13] estimates the nucleation, propagation and interaction of cracks by finding a global minimiser of the total potential energy. Solving this variational problem numerically for discrete cracks can be difficult because the crack path, Γ, evolves with time. In order to overcome this difficulty, a volumetric approximation to the surface integral has been proposed [14]:

$$\int_\Gamma \mathcal{G}\Big(\llbracket \boldsymbol{u} \rrbracket, \kappa\Big)\mathrm{d}A \approx \int_\Omega \mathcal{G}\Big(\llbracket \boldsymbol{u} \rrbracket, \kappa\Big)\gamma_c \mathrm{d}V \tag{7}$$

The phase-field approximation introduces a crack density, γ_c, which depends on a length-scale parameter ℓ and the continuous scalar-valued phase-field, $c \in [0, 1]$, to represent the crack, with $c = 0$ away from the crack and $c = 1$ at the crack [14,16,16]:

$$\gamma_c = \frac{1}{4\ell}\left[c^2 + 4\ell^2|\nabla c|^2\right] \tag{8}$$

which can be derived by approximating the Dirac delta function δ for the strain field at a discontinuity by an exponential function [1,15,16]. Minimising the above functional under the constraints $c(0) = 1$ and $c(\boldsymbol{x}) \to 0$ as $|\boldsymbol{x}| \to \infty$ leads to the Euler equation:

$$c - 4\ell^2\Delta c = 0 \tag{9}$$

The boundary condition, $c(0) = 1$, can be applied either strongly or weakly. It is simpler to impose the boundary condition in a strong format when dealing with less complicated crack patterns. However, for modelling complicated crack patterns a weak format is more suitable [1]. To this end, the Dirichlet constraint is added to the weak form of Eq. (9) in a weighted sense. Using the test function w, the weak form can be written as:

$$\int_\Omega \left(wc + 4\ell^2\frac{\partial w}{\partial x_i}\frac{\partial c}{\partial x_i}\right)\mathrm{d}V + C\frac{4\ell^2}{h}\int_\Omega w(c-1)\delta(x_n)\mathrm{d}V = 0 \tag{10}$$

with C a positive constant that balances the weights of the differential equation and the boundary condition, h a parameter proportional to the mesh size, $x_n = (\boldsymbol{x}-\boldsymbol{x}_c)\cdot\boldsymbol{n}(\boldsymbol{x}_c)$ with $\boldsymbol{n}(\boldsymbol{x})$ the unit vector normal to the fracture surface, and $\boldsymbol{x}_c = \underset{\boldsymbol{y}\in\Gamma}{\operatorname{argmin}}(\|\boldsymbol{y}-\boldsymbol{x}\|)$. The weak form of the phase field equation is obtained after rewriting Eq. (10) as:

$$\int_\Omega \left[w(1+\mathscr{F})c + 4\ell^2\frac{\partial w}{\partial x_i}\frac{\partial c}{\partial x_i}\right]\mathrm{d}V = \int_\Omega w\mathscr{F}\mathrm{d}V \tag{11}$$

with the $\mathscr{F}$ term given by

$$\mathscr{F} = C\frac{4\ell^2}{h}\delta(x_n) \tag{12}$$

From Eq. (11) we observe the dependence of the phase field on the driving force $\mathscr{F}$. If $\mathscr{F} \ll 1$, then $c \to 0$, whereas if $\mathscr{F} \gg 1$, then $c \to 1$. To allow for numerical integration of the constraint term, the Dirac function is approximated as follows:

$$\delta(x_n) = \begin{cases} \frac{1}{h}\left(1 - \frac{|x_n|}{h}\right) & -h \le x_n \le h \\ 0 & \text{otherwise} \end{cases} \tag{13}$$

Equation (11) can be rewritten to yield the strong form:

$$(1 + \mathscr{F})c - 4\ell^2 \Delta c = \mathscr{F} \tag{14}$$

2.3 | Phase-field formulation for cohesive fracture

Combining Eqs (6) and (7), and introducing the auxiliary field $\boldsymbol{w}(\boldsymbol{x})$, which models the jump, results in a volume integral for the potential energy:

$$\Psi_{pot} = \int_{\Omega} \left(\psi_e(\boldsymbol{\varepsilon}^e) + \mathcal{G}\Big(\boldsymbol{w}, \kappa\Big)\gamma_c \right) \mathrm{d}V \tag{15}$$

where $\boldsymbol{\varepsilon}^e$ is the *elastic* strain tensor. The displacement jump is strictly confined to the internal discontinuity Γ and we approximate the discrete displacement jump at $\boldsymbol{x}_c$ using the auxiliary field[1] $\boldsymbol{w}$ as:

$$[\![\boldsymbol{u}]\!](\boldsymbol{x}_c) \approx \int_{-\infty}^{\infty} \boldsymbol{w}(\boldsymbol{x})\gamma_c \mathrm{d}x_n. \tag{16}$$

We emphasise that this is a major deviation from the traditional phase-field approach, in which the crack only exists in a smeared sense. Assuming that the auxiliary field is constant in the direction normal to the fracture leads to:

$$\boldsymbol{w}(\boldsymbol{x}) = \boldsymbol{w}(\boldsymbol{x}_c + x_n \boldsymbol{n}) = \boldsymbol{w}(\boldsymbol{x}_c) \tag{17}$$

with x_n the coordinate along $\boldsymbol{n}$. By inserting Eq. (17) into Eq. (16) we obtain:

$$[\![\boldsymbol{u}]\!](\boldsymbol{x}_c) \approx \int_{-\infty}^{\infty} \boldsymbol{w}(\boldsymbol{x})\gamma_c \mathrm{d}x_n = \boldsymbol{w}(\boldsymbol{x}_c) \int_{-\infty}^{\infty} \gamma_c \mathrm{d}x_n = \boldsymbol{w}(\boldsymbol{x}_c) \tag{18}$$

which shows that $\boldsymbol{w}(\boldsymbol{x})$ represents the crack opening at the closest point $\boldsymbol{x}_c$ on the discrete internal boundary. The constraint that the auxiliary field is constant in the direction normal to the crack is enforced weakly through the addition of a penalty term in the internal energy functional:

$$\Psi_{pot} = \int_{\Omega} \left(\psi_e(\boldsymbol{\varepsilon}^e) + \mathcal{G}\Big(\boldsymbol{w}, \kappa\Big)\gamma_c + \frac{1}{2}\alpha \Big| \frac{\partial \boldsymbol{w}}{\partial x_n} \Big|^2 \right) \mathrm{d}V \tag{19}$$

with α a penalty parameter[1].

The weak form of the cohesive phase-field problem is obtained by taking variations of the displacement field $\boldsymbol{u}$ and the auxiliary field $\boldsymbol{w}$, while keeping the phase-field constant

$$\delta\Psi_{pot} = \int_{\Omega} \left(\sigma_{ij}\delta\varepsilon^e_{ij} + t_i\Big(\boldsymbol{w}, \kappa\Big)\gamma_c \delta w_i + \alpha \frac{\partial w_i}{\partial x_n} \frac{\partial \delta w_i}{\partial x_n} \right) \mathrm{d}V = \delta\Psi_{ext} \tag{20}$$

where in the absence of body forces,

$$\delta\Psi_{ext} = \int_{\partial\Omega} h_i \delta u_i \mathrm{d}A \tag{21}$$

with h_i representing the traction along the Neumann boundary $\partial\Omega_{h_i}$. In Eq. (20), $\sigma_{ij} = \frac{\partial \psi_e}{\partial \varepsilon^e_{ij}}$ are the components of the Cauchy stress and $t_i = \frac{\partial \mathcal{G}}{\partial w_i}$ are the cohesive tractions.

The elastic strain tensor, $\boldsymbol{\varepsilon}^e$, is related to the displacement field $\boldsymbol{u}$ and the auxiliary field $\boldsymbol{w}$ via

$$\varepsilon^e_{ij} = u_{(i,j)} - \mathrm{sym}\Big(w_i n_j\Big)\gamma_c \tag{22}$$

In Eq. (22), the first term is the symmetric part of the gradient of the displacement field and the second term is the strain caused by the displacement jump. Substituting the variation of Eq. (22) into Eq. (20) we obtain the following weak forms

$$\int_{\Omega} \sigma_{ij}\delta u_{ij} \mathrm{d}V = \int_{\partial\Omega} h_i \delta u_i \mathrm{d}A \tag{23}$$

and

$$\int_{\Omega} \Big(-\gamma_c \sigma_{ij} \mathrm{sym}(w_i n_j) + \gamma_c t_i \delta w_i + \alpha \frac{\partial w_i}{\partial x_n} \frac{\partial \delta w_i}{\partial x_n} \Big) \mathrm{d}V = 0 \tag{24}$$

We finally use Eqs (23) and (24) to derive the governing equations in a strong format:

$$\begin{cases} \frac{\partial \sigma_{ij}}{\partial x_j} = 0 & \boldsymbol{x} \in \Omega \\ \sigma_{ij} n_j = h_i & \boldsymbol{x} \in \partial\Omega \end{cases} \tag{25}$$

and

$$\begin{cases} \gamma_\ell \Big(t_i - \sigma_{ij} n_j \Big) = \alpha \frac{\partial^2 w_i}{\partial x_n^2} & \boldsymbol{x} \in \Gamma_c \\ \frac{\partial w_i}{\partial x_n} = 0 & \boldsymbol{x} \in \partial\Gamma_c \end{cases} \tag{26}$$

It is noted that $\Gamma_c = \Big\{ \boldsymbol{x} \in \Omega \;\Big|\; c(\boldsymbol{x}) > tol \Big\}$ marks the smeared internal discontinuity, with $tol \ll 1$ a small tolerance.

3 | DISCRETISATION

Different from earlier work on cohesive phase-field models [1,22,23], we use NURBS for the spatial discretisation [34]. NURBS basis functions can be constructed for an arbitrarily high degree of continuity, and although the isotropic phase-field model permits the use of classical C^0-continuous elements, the use of a smooth basis is beneficial, as the stresses are represented more accurately [35]. Bézier extraction constructs the minimal set of Bézier elements defining a NURBS [36]. A Bézier element is a region of the physical domain in which the basis functions are C^{p-1}-continuous. Furthermore, Bézier extraction also builds an extraction operator for each Bézier element that maps a Bernstein polynomial basis defined on the Bézier element to the global smooth basis.

For the discretisation of the weak form of Eq. (11) we approximate the phase field as:

$$c(\boldsymbol{x}) = \boldsymbol{N}_c(\boldsymbol{x}) \boldsymbol{a}_c \tag{27}$$

where $\boldsymbol{a}_c$ is an array which contains the control variables of the phase field and $\boldsymbol{N}_c$ contains the NURBS basis functions. By differentiation, we obtain:

$$\frac{\partial c}{\partial \boldsymbol{x}}(\boldsymbol{x}) = \boldsymbol{B}_c(\boldsymbol{x}) \boldsymbol{a}_c \tag{28}$$

where $\boldsymbol{B}_c$ contains the gradients of the basis functions. Using a Galerkin approach, the following system then results from Eq. (11):

$$\left(\int_\Omega \Big[w(1+\mathscr{F}) \boldsymbol{N}_c^T \boldsymbol{N}_c + 4\ell^2 \boldsymbol{B}_c^T \boldsymbol{B}_c \Big] \mathrm{d}V \right) \boldsymbol{a}_c = \int_\Omega w \mathscr{F} \mathrm{d}V \tag{29}$$

The parameter h in the definition of the driving force $\mathscr{F}$, Eq. (12), directly relates to the mesh size. When the system (29) has been solved, the crack density, Eq. (8), follows from:

$$\gamma_c = \boldsymbol{a}_c^T \left[\frac{1}{4\ell} \boldsymbol{N}_c^T \boldsymbol{N}_c + \ell \boldsymbol{B}_c^T \boldsymbol{B}_c \right] \boldsymbol{a}_c . \tag{30}$$

Eqs (25) and (26) are solved monolithically for a given phase field c. The discretisation of the displacement field is given by:

$$\boldsymbol{u} = \boldsymbol{N}_u \boldsymbol{a}_u \,, \qquad \mathrm{sym}\left(\frac{\partial \boldsymbol{u}}{\partial \boldsymbol{x}} \right) = \boldsymbol{B}_u \boldsymbol{a}_u \tag{31}$$

while that of the auxiliary field reads:

$$\boldsymbol{w} = \boldsymbol{N}_w \boldsymbol{a}_w \,, \quad \mathrm{sym}\Big(\boldsymbol{w} \otimes \boldsymbol{n} \Big) = \boldsymbol{B}_w \boldsymbol{a}_w \,, \quad \frac{\partial \boldsymbol{w}}{\partial x_n} = \boldsymbol{G}_w \boldsymbol{a}_w \tag{32}$$

From this, the following system, which is non-linear due to the cohesive law, results:

$$\begin{aligned} \boldsymbol{f}_{int,u}(\boldsymbol{a}_u, \boldsymbol{a}_w) &= \boldsymbol{f}_{ext,u} \\ \boldsymbol{f}_{int,w}(\boldsymbol{a}_u, \boldsymbol{a}_w) &= \boldsymbol{0} \end{aligned} \tag{33}$$

with the internal force vectors defined as:

$$\boldsymbol{f}_{int,u} = \int_\Omega \boldsymbol{B}_u^T \Big(\boldsymbol{C} \boldsymbol{B}_u \boldsymbol{a}_u - \gamma_c \boldsymbol{C} \boldsymbol{B}_w \boldsymbol{a}_w \Big) \mathrm{d}V \tag{34}$$

and

$$\boldsymbol{f}_{int,w} = \int_{\Omega} \Big(-\gamma_c \boldsymbol{B}_w^T \Big(\boldsymbol{C}\boldsymbol{B}_u \boldsymbol{a}_u - \gamma_c \boldsymbol{C}\boldsymbol{B}_w \boldsymbol{a}_w \Big) + \gamma_c \boldsymbol{N}_w^T \boldsymbol{t}(\boldsymbol{w}) + \alpha \boldsymbol{G}_w^T \boldsymbol{G}_w \boldsymbol{a}_w \Big) \mathrm{d}V \tag{35}$$

with $\boldsymbol{C}$ the elasticity matrix. The system of Eq. (33) is solved using a standard Newton-Raphson procedure with the tangent stiffness matrix:

$$\boldsymbol{K} = \begin{bmatrix} \boldsymbol{K}_{uu} & \boldsymbol{K}_{uw} \\ \boldsymbol{K}_{wu} & \boldsymbol{K}_{ww} \end{bmatrix} \tag{36}$$

with

$$\boldsymbol{K}_{uu} = \frac{\partial \boldsymbol{f}_{int,u}}{\partial \boldsymbol{a}_u} = \int_{\Omega} \boldsymbol{B}_u^T \boldsymbol{C}\boldsymbol{B}_u \mathrm{d}V \tag{37}$$

$$\boldsymbol{K}_{uw} = \frac{\partial \boldsymbol{f}_{int,u}}{\partial \boldsymbol{a}_w} = \int_{\Omega} -\gamma_c \boldsymbol{B}_u^T \boldsymbol{C}\boldsymbol{B}_w \mathrm{d}V \tag{38}$$

$$\boldsymbol{K}_{wu} = \boldsymbol{K}_{u,w}^T = \int_{\Omega} -\gamma_c \boldsymbol{B}_w^T \boldsymbol{C}\boldsymbol{B}_u \mathrm{d}V \tag{39}$$

$$\boldsymbol{K}_{ww} = \frac{\partial \boldsymbol{f}_{int,w}}{\partial \boldsymbol{a}_w} = \int_{\Omega} \left(\gamma_c^2 \boldsymbol{B}_w^T \boldsymbol{C}\boldsymbol{B}_w + \gamma_c \boldsymbol{N}_w^T \frac{\partial \boldsymbol{t}}{\partial \boldsymbol{w}} + \alpha \boldsymbol{G}_w^T \boldsymbol{G}_w \right) \mathrm{d}V \tag{40}$$

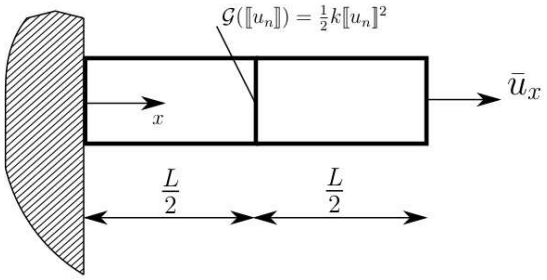

FIGURE 1 Bar with an elastic interface, $\mathcal{G} = \frac{1}{2}k[\![\boldsymbol{u}]\!]^2$, at the centre.

4 | ANALYSIS AND DISCUSSION

We now investigate the sensitivity of the cohesive phase-field formulation with respect to the discretisation and the order of the continuity of the basis functions for a one-dimensional test problem. In all examples the constant $C = 10^1$, which enforces the Dirichlet constraint in a weak sense, while the tolerance which marks the smeared internal discontinuity $tol = 10^{-3}$.

4.1 | Discretisation sensitivity

We consider a one-dimensional domain of unit length with a modulus of elasticity $E = 1$ and an elastic interface as depicted in Figure 1. The energy in the interface, with an stiffness $k = 1$, is assumed as:

$$\mathcal{G} = \frac{1}{2}k[\![\boldsymbol{u}]\!]^2 = \frac{1}{2}kw^2 \tag{41}$$

so that $t = kw$. The length scale parameter $\ell = L/20$ and $\alpha = 0.1$.

Figures 2(a) and 2(b) show the corresponding stress field and the strain contributions when all fields are discretised using piecewise linear basis functions. The solution of the stress field reveals an oscillatory behaviour. This can be explained by considering the elastic strain, which, for this one-dimensional case, is given by[1]:

$$\varepsilon^e = \frac{\mathrm{d}u}{\mathrm{d}x} - \gamma_c w = \frac{\mathrm{d}u}{\mathrm{d}x} - \left[\frac{c^2}{4\ell} + \ell \Big(\frac{\mathrm{d}c}{\mathrm{d}x} \Big)^2 \right] w \tag{42}$$

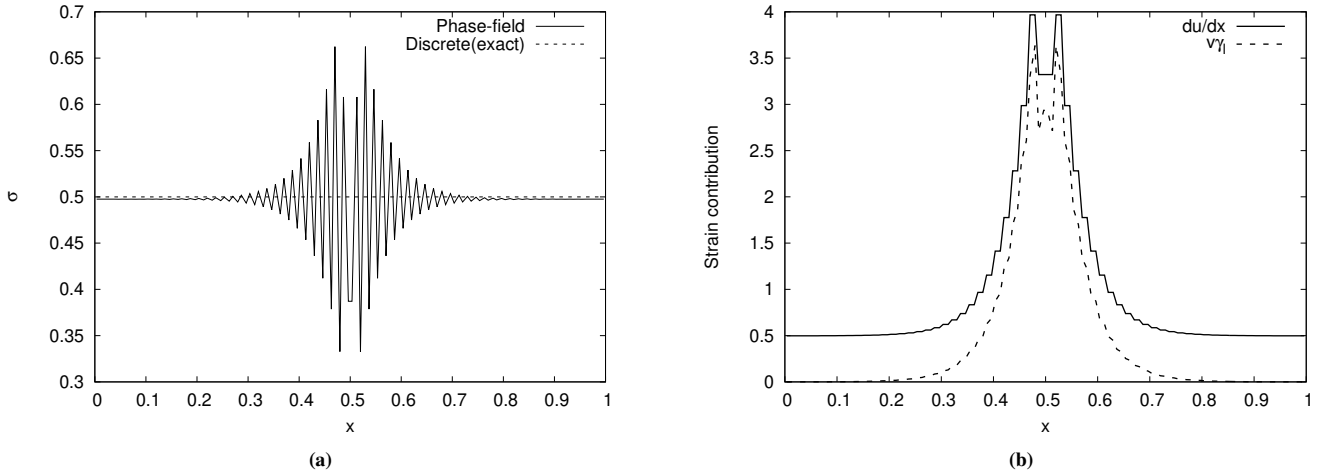

FIGURE 2 (a) Stress field obtained using a discretisation based on piecewise linear NURBS for all fields; (b) Strain contributions for a discretisation based on piecewise linear NURBS for all fields.

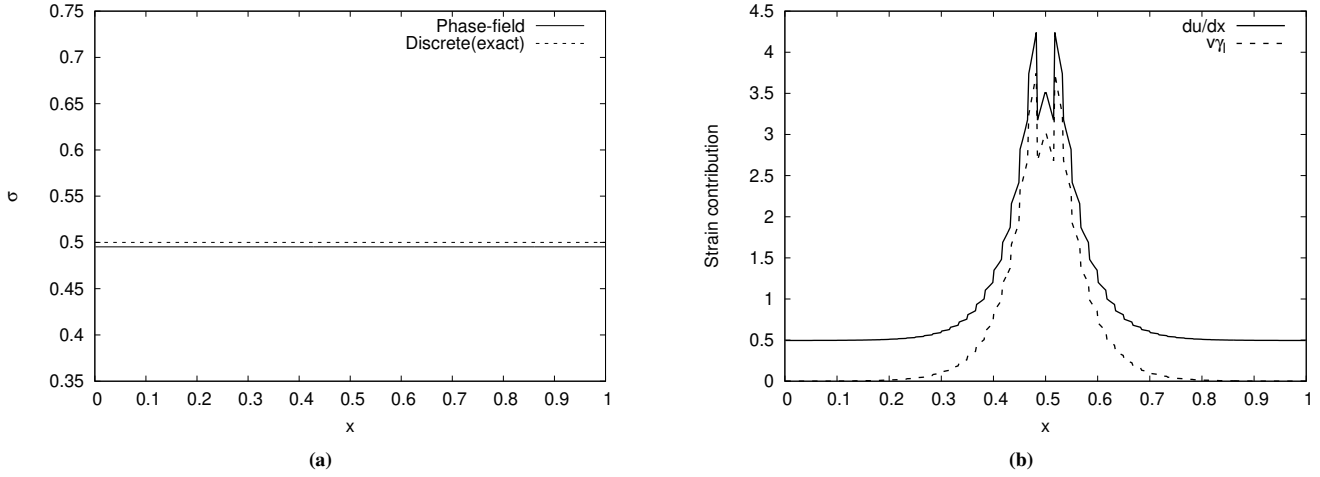

FIGURE 3 (a) Stress field obtained using a discretisation based on piecewise linear NURBS for the phase field and the displacement jump field, and cubic NURBS for the displacement field with C^0-continuous basis functions across the elements; (b) Strain contributions.

Since the displacement, u, is approximated by a piecewise linear function, the strain distribution is piecewise constant, Figure 2(b). When we consider the contribution to the elastic strain of the jump field, we observe that γ_c has a quadratic contribution and w is approximated by piecewise linear functions. The jump is forced to be constant in the direction perpendicular to the discontinuity, which effectively makes the contribution of the jump field to the strain quadratic. The stress oscillations observed in Figure 2(a) are a direct consequence of the mismatch in the approximation orders of the two strain contributions.

From Eq. (42), it is observed that, when the order of the NURBS for the displacement field is taken as equal to three, the orders of the strain contributions do match, see Figure 3(b). Figure 3(a) shows that a discretisation with piecewise linear basis functions for the phase field and the displacement jump field, and cubic NURBS for the displacement field *with C^0-continuous basis functions across* the elements, fully eliminates the stress oscillations. This observation is in line with conclusions reached when using Lagrange polynomials instead of NURBS[1]. It is noted that the solution slightly deviates from the exact solution, because the internal boundary is enforced weakly using the constant C. Upon mesh refinement the difference disappears.

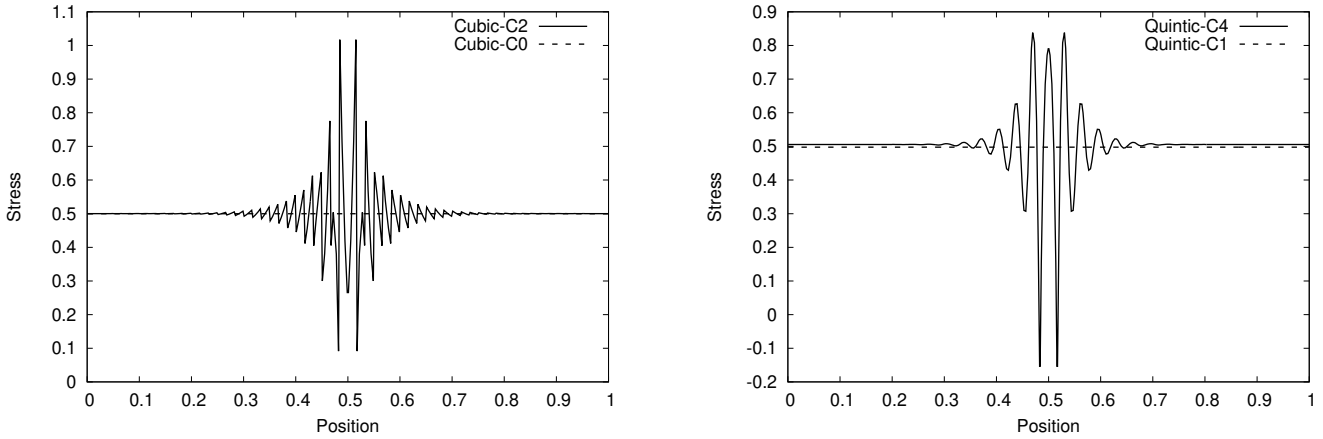

FIGURE 4 (a) Stress field obtained using a discretisation based on piecewise linear NURBS for the phase field and the displacement jump field, and cubic NURBS for the displacement field with C^0-continuity across the elements. (b) Stress field obtained using a discretisation based on quadratic NURBS for the phase field and the displacement jump field, and quintic NURBS for the displacement field with C^1-continuity across the elements.

4.2 | Sensitivity to the order of continuity

Figure 4(a) shows that changing to NURBS which have C^2-continuity for the displacement field *across* element boundaries re-introduces stress oscillations (drawn line). This can be explained by considering Eq. (42). The second term, $\gamma_c w$, is approximated by C^0-continuous basis functions across the elements. In order to have consistency in the order of continuity, the first term, $\frac{\mathrm{d}u}{\mathrm{d}x}$, must be expressed by C^0-continuous basis functions across the elements. This can be achieved using knot insertion[37,38]. Then, the stress oscillations again disappear, see the dashed line in Figure 4(a). This behaviour is reminiscent of that of isogeometric interface elements, where the introduction of C^0 lines also eliminated traction oscillations, at least when using Newton-Cotes integration as is customary in standard (Lagrange) interface elements[39].

The stress oscillations can also be eliminated by considering a higher-order interpolation for the displacements, for example using quintic NURBS in combination with having C^1 continuity for all fields at the element boundaries, and using quadratic NURBS for the phase field and the displacement jump field. This is shown by the dashed line in Figure 4(b). However, due to the constraint on the jump, the optimal choice is still C^0 continuity for all fields at the element boundaries. As also shown in Figure 4(b), the use of the C^1-continuous basis functions can reduce oscillations significantly and more accurate stress fields are obtained compared to standard finite elements.

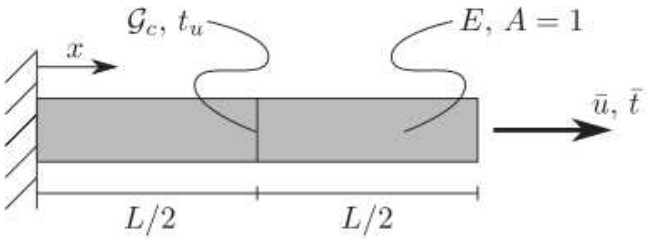

FIGURE 5 Bar with a cohesive interface at the centre.

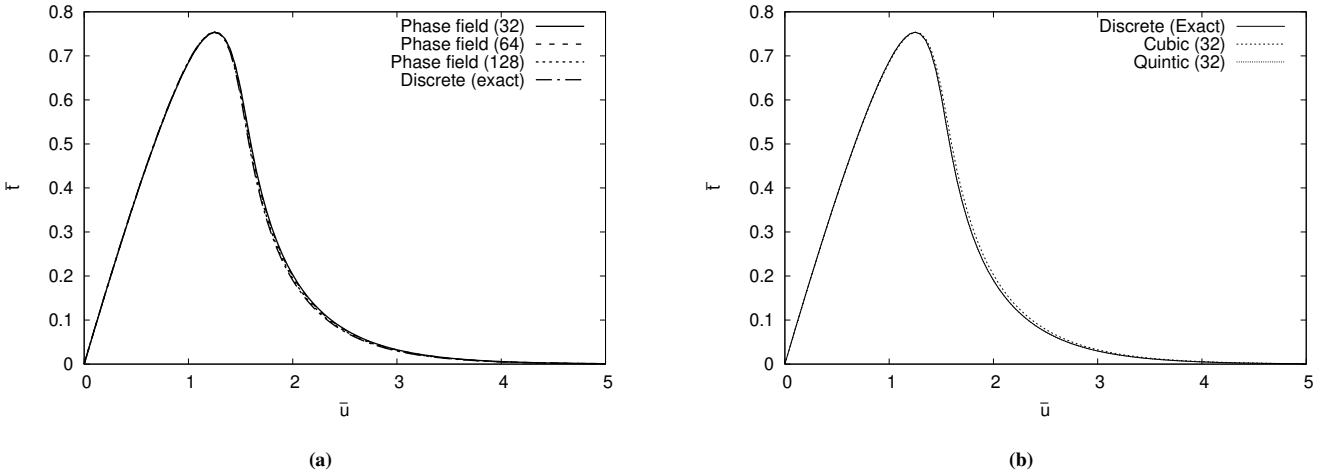

(a) **(b)**

FIGURE 6 Force-displacement curve for the one-dimensional cohesive fracture of a rod. (a) Piecewise linear NURBS are used for the phase field and the displacement jump field, and piecewise cubic NURBS is utilised for the displacement field. (b) Comparison between quintic and cubic NURBS used for the displacement field.

5 | CASE STUDIES

5.1 | Cohesive fracture of a rod

We consider a one-dimensional rod with a cohesive interface, see Figure 5. The length of the rod is $L = 1$ and the modulus of elasticity $E = 1$. The interface energy is taken as[5]:

$$\mathcal{G} = \mathcal{G}_c \left[1 - \left(1 + \frac{[\![u]\!]}{\delta_n} \right) \exp(-\frac{[\![u]\!]}{\delta_n}) \right] \qquad t = \mathcal{G}_c \frac{[\![u]\!]}{\delta_n^2} \exp(-\frac{[\![u]\!]}{\delta_n}) \tag{43}$$

with $\delta_n = \mathcal{G}_c/(t_u e)$, $e = \exp(1)$, from which the traction follows as

$$t = \mathcal{G}_c \frac{[\![u]\!]}{\delta_n^2} \exp\left(- \frac{[\![u]\!]}{\delta_n} \right) \tag{44}$$

The fracture strength and the fracture energy are taken as $t_u = 0.75$ and $\mathcal{G}_c = 1$, respectively. The length scale parameter $\ell = L/20$ and the penalty parameter $\alpha = 0.1$. The rod is discretised using linear NURBS for the phase field and the displacement jump field, and cubic NURBS with C^0-continuity at the element boundaries for the displacement field. The equilibrium path is traced using displacement control with a Newton-Raphson solver. Figure 6(a) shows the response for various mesh refinements of the phase field (32, 64 and 128 Bézier elements) and a comparison is given with the exact solution to the discrete problem. Already the coarse (32 element) mesh yields almost the exact solution, which is a direct consequence of the use of NURBS basis functions. Even more accurate results can be obtaind using higher-order basis functions, e.g. quintic NURBS for the displacement and quadratic NURBS for the phase field and the displacement jump, see Figure 6(b).

5.2 | One-dimensional bar in a two-dimensional domain

We now consider a bar with $L = 1$, $\ell = 0.1$ and $c = 1$ as shown in Figure 7. Cubic NURBS basis functions are used to approximate the displacement, and the phase field and the crack opening field are approximated using linear basis functions. C^0 continuity is enforced at all element boundaries. A two-dimensional setting is used, but a purely one-dimensional stress is obtained by setting Poisson's ratio $\nu = 0$ and by prescribing all shear components of the smeared jump to zero: $w_s = w_y = 0$. The other parameters are as in the purely one-dimensional case.

A 10×10 structured mesh is used for the baseline solution. As stated in the Introduction stress oscillations have been observed when displacing nodes to yield an unstructured mesh. In order to further examine this issue some nodes have been displaced in subsequent (linear) calculations. Figure 8 depicts three meshes, with a high, a medium and a low degree of irregularity, i.e.

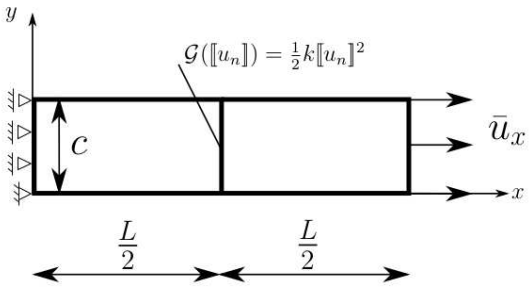

FIGURE 7 Bar with an elastic interface, $\mathcal{G} = \frac{1}{2}k[\![\boldsymbol{u}]\!]^2$, in the centre.

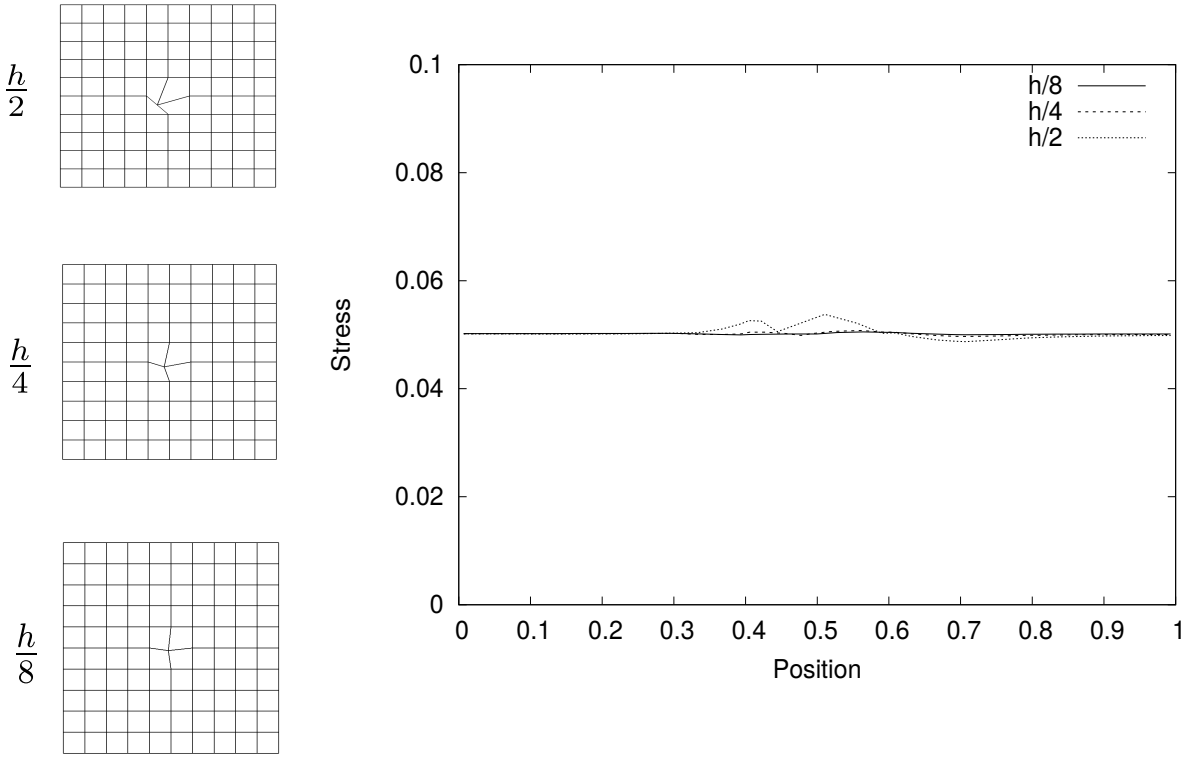

FIGURE 8 Three Bézier meshes with a high, a medium and a low degree of irregularity and the resulting stress profiles.

the initial displacement of the centre node of the distorted patch is $h/2$, $h/4$ and $h/8$, respectively. As shown in Figure 8, even the most irregular mesh results in very limited stress oscillations. In fact, different from previous hypotheses[23], it turns out that the oscillations are due to the fact that the Dirichlet constraints are weakly imposed in the current phase-field approach to cohesive fracture. Moreover, improving the approximation reduces the oscillations considerably, as the present oscillations are much smaller than when Lagrange interpolation functions were used[23]. In sum, with a suitable, higher-order and matched approximation of the three fields, an acceptable performance of the weak imposition of the Dirichlet constraints is obtained.

Next, we replace the elastic interface with the cohesive interface used in the previous one-dimensional numerical simulation. The force-displacement curves for the structured and the unstructured meshes are identical, see Figure 9, giving further evidence of the good performance of the weakly imposed Dirichlet constraints.

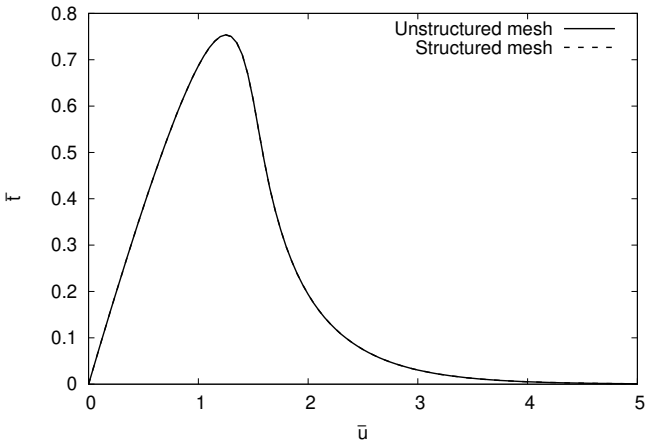

FIGURE 9 Force-displacement curves for the structured mesh and the irregular $(h/2)$ mesh.

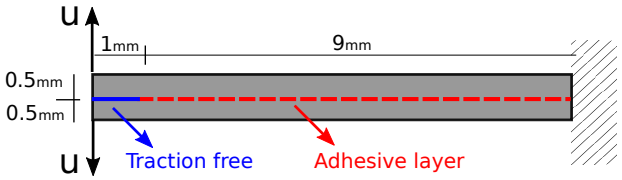

FIGURE 10 Geometry of the delamination peel test

5.3 | Delamination peel test

To investigate the applicability of the formulation in a real two-dimensional problem, we consider the delamination peel test of Figure 10. The test consists of two cantilever beams that are 10 mm long and 0.5 mm high, and are connected over 90% of their length by means of an adhesive layer. Upon increasing the externally applied displacement, u, this adhesive layer will debond progressively. The bulk material is modelled as a linear isotropic material with a modulus of elasticity $E = 100$ MPa and a Poisson's ratio $\nu = 0.3$. Plane-strain conditions are assumed. The behaviour of the adhesive layer is modelled using the Xu-Needleman decohesion relation[5], which, for mode-I crack opening, reduces to Eq. (43). The fracture strength and fracture energy are taken as $t_u = 1$ MPa and $\mathcal{G}_c = 0.1$ N/mm, respectively. For the length scale parameter, we take $\ell = 0.05$ mm and $\ell = 0.1$ mm, while $\alpha = 1$ MPa.

Figure 11 shows the force-displacement curves for different refinement levels, and are in good agreement with results obtained before[1]. Evidently, the smaller value for the length scale parameter, ℓ, yields a higher peak load, see Figure 12, which confirms that it should be regarded as a material parameter rather than a numerical parameter. Finally, Figure 13 shows the stress field at three progressive stages of the peel test as well as the deformed geometry.

5.4 | Peel test with propagating interface

We reconsider the peel test, but now with only a traction-free pre-crack as shown in Figure 14. The crack is allowed to propagate into the bulk material when the displacement load is increasing. The material properties are taken the same as before, which also holds for the decohesion relation. Only the larger value of the internal length scale, $\ell = 0.1$ mm, has been used.

As alluded to in the Introduction, the present formulation seems deficient in modelling the propagation of cracks in arbitrary directions, and the ad-hoc crack evolution model used by Verhoosel and de Borst[1] was used for crack nucleation and propagation. First, a pre-crack is defined, Γ^0, which is represented by a set of position and normal vectors sampled along the interface:

$$\mathcal{S}^0 \subset \left\{ \left(\boldsymbol{x}, \boldsymbol{n}(\boldsymbol{x}) \right) \in \Gamma^0 \right\} \tag{45}$$

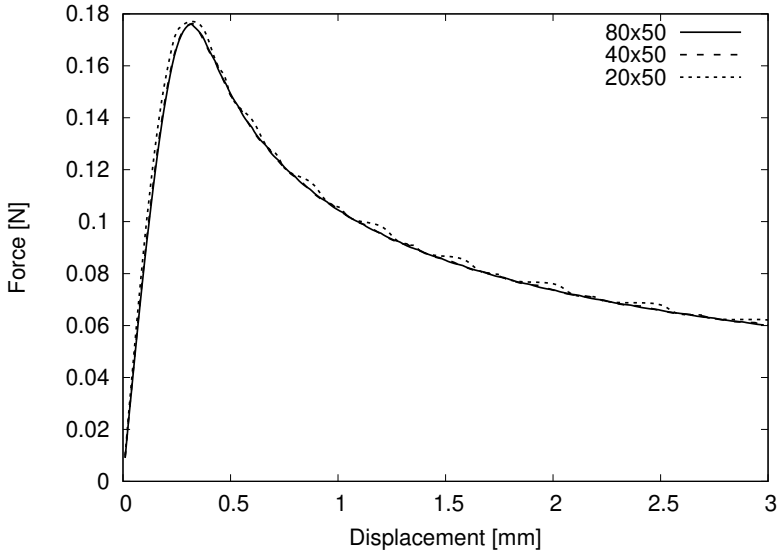

FIGURE 11 Force-displacement diagram for the delamination peel test computed for various meshes.

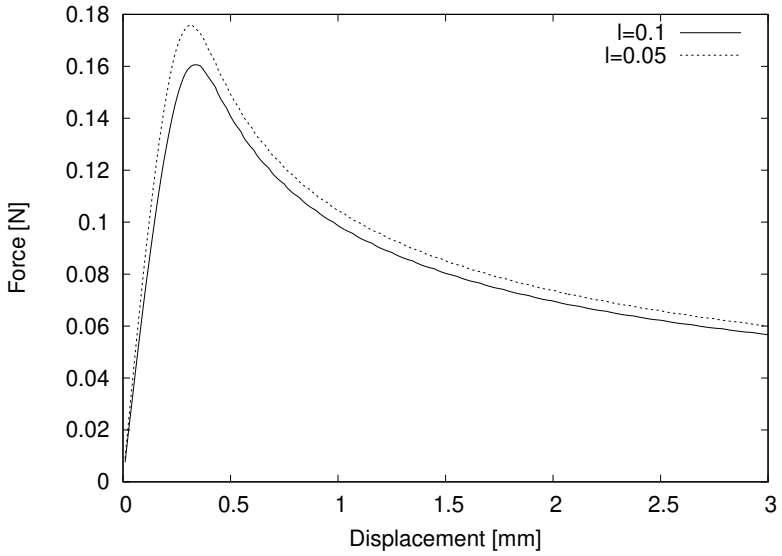

FIGURE 12 Force-displacement curve for the delamination peel test

The point set $\mathcal{S}^0$ is used to evaluate the driving force, Eq. (12). Then, the phase-field problem, Eq. (29) is solved. After obtaining the smeared crack representation by this field, γ_c, we compute the displacements and displacement jumps for the next time step through the solution of Eq. 33. Now, we are able to compute the nucleation criterion, $\Sigma_{nuc}(\sigma_i) > t_u$, in all integration points and extend the point set $\mathcal{S}^t$ of the previous time step with the points for which the nucleation criterion is now satisfied:

$$\mathcal{S}^{t+\Delta t} = \mathcal{S}^t \cup \left\{ \left(\boldsymbol{x}_i, \boldsymbol{n}_i \right) \middle| \Sigma_{nuc}(\sigma_i) > t_u \ , \ i \in \mathcal{I}_{int} \right\} \tag{46}$$

where σ_i are the stresses in all integration points of the set $\mathcal{I}_{int}$. The nucleation/propagation model also yields a normal vector, $\boldsymbol{n}_i$, in all points where the criterion is met. The normal vector is calculated by means of a maximum principal stress criterion as is commonly done in the cohesive-zone approach. In the example the crack has been forced to remain straight by constraining the normal vector to be vertical.

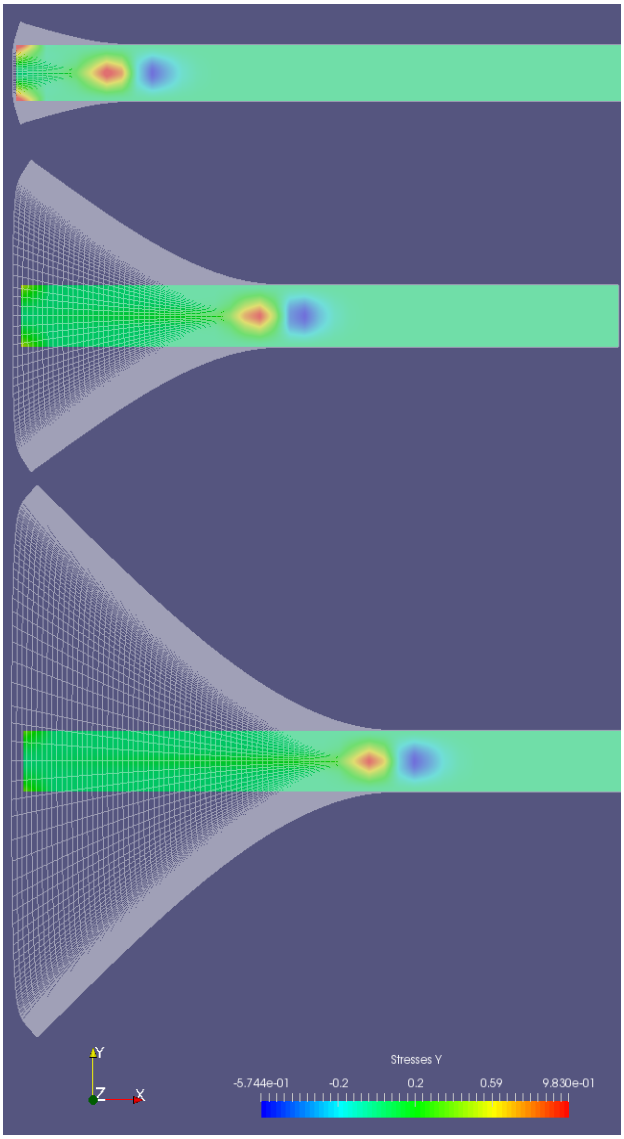

FIGURE 13 Deformed geometry and σ_{yy} stress field at three progressive stages in the delamination peel test

Figure 15 shows the phase field at three progressive stages in the peel test with propagating crack. The force-displacement curves for the peel test with propagating crack computed for various meshes are depicted in Figure 16.

5.5 | Fibre-epoxy debonding experiment

A fibre with a 5 μm radius embedded in a 30 × 30 μm square block of epoxy is considered, see Figure 17[37]. The specimen is loaded in the horizontal direction by gradually increasing the displacement $\bar{u}$ of the left and right edges. The symmetry of the specimen permits restriction of the computational domain to the top right quadrant of the specimen, in combination with horizontal rollers along the x-axis and vertical rollers along the y-axis.

The fibre as well as the epoxy are modelled as linear elastic. For the epoxy a Young's modulus $E = 4.3$ GPa and a Poisson's ratio $\nu = 0.34$ have been used. For the fibre the moduli are: $E = 22.5$ GPa and $\nu = 0.2$. The traction at the interface is assumed

FIGURE 14 Geometry of the delamination peel test with a propagating discontinuity

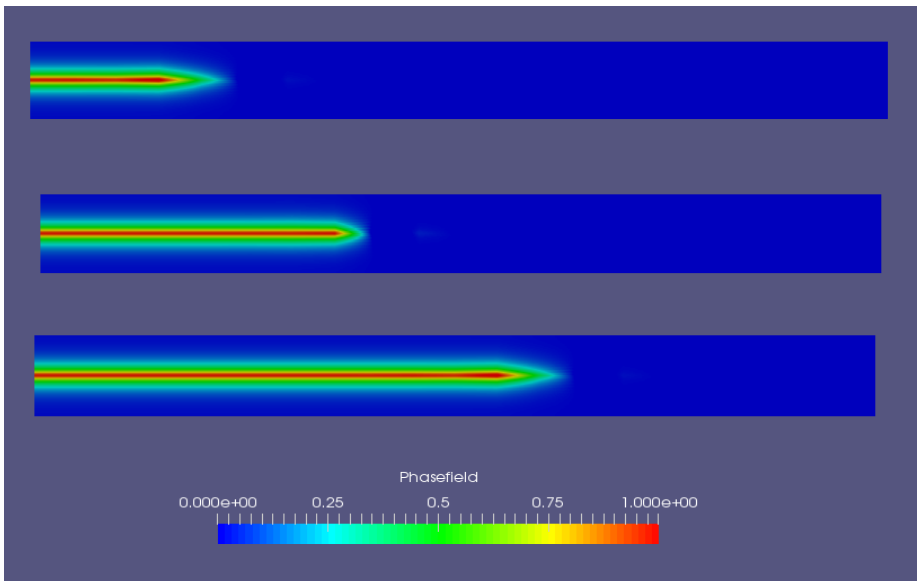

FIGURE 15 Phase field at three progressive stages in the peel test with propagating crack.

to be given by the Xu-Needleman relation[5].

$$t_n = \frac{\mathcal{G}_c}{\delta_n}\frac{[\![u_n]\!]}{\delta_n}\exp\Big(-\frac{[\![u_n]\!]}{\delta_n}\Big)\exp\Big(-\frac{[\![u_s]\!]^2}{\delta_s^2}\Big) \tag{47}$$

and

$$t_s = \frac{2\mathcal{G}_c}{\delta_s}\frac{[\![u_s]\!]}{\delta_s}\Big(1+\frac{[\![u_n]\!]}{\delta_n}\Big)\exp\Big(-\frac{[\![u_n]\!]}{\delta_n}\Big)\exp\Big(-\frac{[\![u_s]\!]^2}{\delta_s^2}\Big) \tag{48}$$

for loading. The fracture strength and fracture energy in normal (mode I) and in shear (mode II) are taken as $t_u = 50$ MPa and $\mathcal{G}_c = 4\times10^{-3}$ N/mm, respectively. The parameters δ_n and δ_s are related to the fracture strength and the fracture toughness via $\delta_n = \mathcal{G}_c/(t_u e)$ and $\delta_s = \mathcal{G}_c/\Big(t_u\sqrt{\frac{1}{e}}\Big)$. The loading condition is checked on the basis of the history parameter κ and the loading function $f = \sqrt{\langle[\![u_n]\!]\rangle^2 + \beta^{-1}[\![u_s]\!]^2} - \kappa$, with $\langle[\![u_n]\!]\rangle = \frac{1}{2}\Big(|[\![u_n]\!]| + [\![u_n]\!]\Big)$ and $\beta = 2.3$ the mode-mixity parameter. The history function f evolves according to the Kuhn-Tucker conditions

$$f \le 0 \qquad \dot\kappa \ge 0 \qquad \dot\kappa f = 0 \tag{49}$$

In the case of unloading ($f < 0$), the traction components are related to the crack opening through the secant stiffnesses.

The debonding between fibre and epoxy leads to a structural softening. When the fibre and epoxy have fully debonded, the force increases again as the epoxy continues to carry load, Figure 18. The debonding process is visualised in Figure 19. From the contour plot, Figure 19(a), it is observed that the σ_{xx} component is continuous in either subdomain, as are the other stress components. Figure 19(b) shows the normal and the tangential components of the displacement jump along the fibre-matrix interface at $\bar u = 0.165$ μm for the 4×16 mesh.

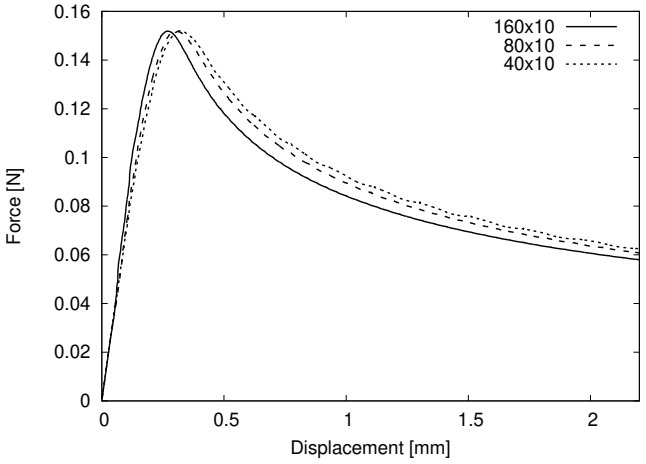

FIGURE 16 Force-displacement diagrams for the peel test with a propagating crack computed for various meshes.

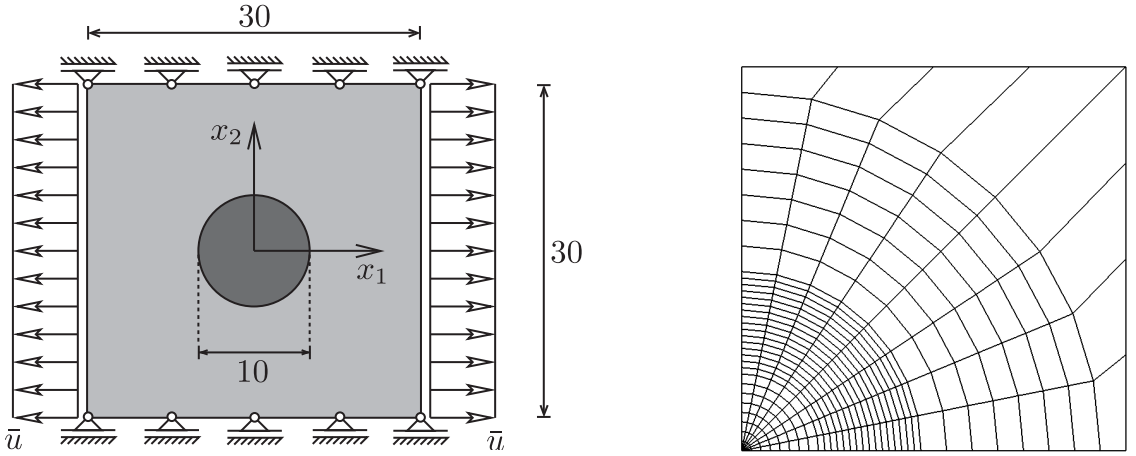

(a) **(b)**

FIGURE 17 (a) A fibre with a circular cross section embedded in a square block of epoxy. Dimensions in μm; (b) 8×32 element mesh used for the fibre-epoxy simulations.

6 | CONCLUDING REMARKS

We have examined a phase-field method for cohesive fracture. The salient characteristic of the approach is that the crack opening is modelled explicitly, in addition to the displacement field and the phase field. The phase field therefore has the sole purpose of locating the crack. Different from the phase-field approach for brittle fracture, separate criteria for crack nucleation and crack propagation are therefore needed. While being straightforward when simple configurations are considered, like debonding along a straight, pre-defined surface, this necessitates ad-hoc rules for nucleation and propagation. In this sense, the current formulation of the cohesive phase-field model is therefore still immature. Indeed, the phase field evolution is now decoupled from the displacement field. Although this is a reasonable assumption for adhesive interfaces, the nucleation and propagation of cracks with an arbitrary topology should follow from the energy balance of a fully coupled model.

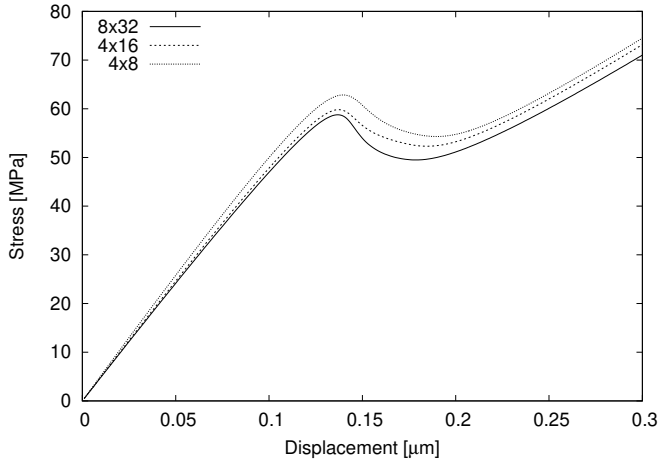

FIGURE 18 Stress-displacement curves for the fibre-epoxy system determined using various meshes. The stress component σ_{xx} at x = (15, 0) μm is plotted *vs* the horizontal displacement $\bar{u}$.

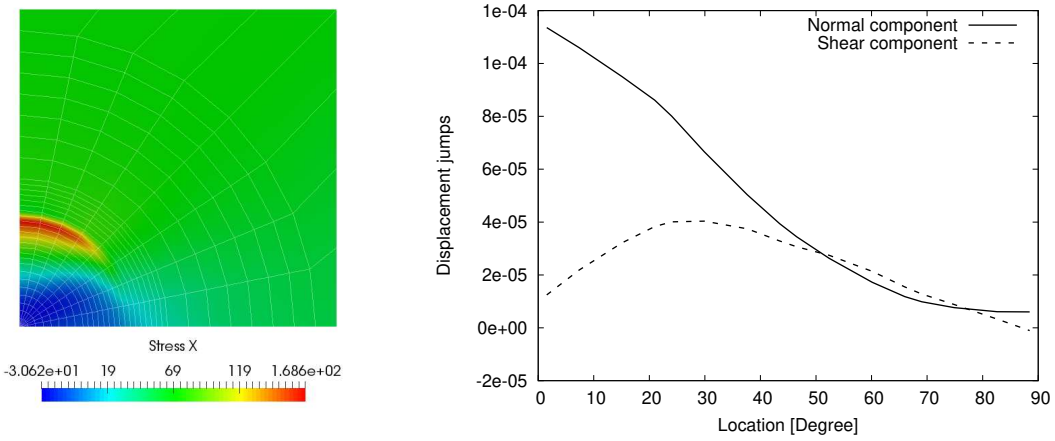

(a) **(b)**

FIGURE 19 (a) Contour plot showing the σ_{xx} stress in the fibre-epoxy system at $\bar{u} = 0.165$ μm using the 8×32 element discretisation; (b) the normal and the tangential components of the displacement jump along the fibre-matrix interface at $\bar{u} = 0.165$ μm using the 4×16 mesh. The angle is measured from the horizontal x-axis.

The current phase-field formulation for cohesive fracture requires that the phase field at the centre of the crack is imposed as a Dirichlet boundary condition, either strongly or weakly. A weak imposition of the boundary condition is more generally applicable[1]. However, its use in unstructured meshes leads to stress oscillations[22,23]. This issue has now been examined in detail, and disappears rather quickly when higher-order approximations are used. Indeed, different from previous investigations[22,23], where Lagrange interpolations were used, the current investigation exploits Non-Uniform Rational B-Splines (NURBS), which are very beneficial in this context. Non-linear calculations involving decohesion show that the differences between structured and unstructured meshes are indistinguishable, thereby validating the weak imposition of the boundary condition for the phase field at the centre of the crack.

More in general, NURBS yield a considerably higher accuracy, or put differently, the same accuracy can be obtained with less elements, as has been found also in the current simulations. The cohesive phase-field approach, however, imposes some restrictions. In particular, continuity at element boundaries should be reduced in order that the interpolations between the three fields continue to match. It turns out that a reduction to C^0-continuity for all fields is the optimal choice.

The approach has been illustrated for a number of boundary value problems, all showing a good behaviour. It is noteworthy that coarser meshes could be used than is usual in phase-field simulations of brittle fracture, which is due to the fact that the displacement jump is interpolated explicitly rather than being considered in a smeared sense, and the fact that cohesive fracture removes the stress singularity at the crack tip which is inherent in brittle fracture. Of particular interest is the case of debonding of a hard, circular fibre in a soft epoxy matrix, where the ability of NURBS to exactly capture the circular geometry of the fibre is an additional advantage. Good results have been obtained which well match results from a discrete cohesive-zone model[37].

Acknowledgement

Financial support from the European Research Council (Advanced Grand 664734 "PoroFrac") is gratefully acknowledged.

References

1. Verhoosel CV, de Borst R. A phase-field model for cohesive fracture. *International Journal for Numerical Methods in Engineering* 2013; 96: 43–62.

2. Rots JG. Smeared and discrete representations of localized fracture.. *International Journal of Fracture* 1991; 51: 45–59.

3. Allix O, Ladevèze P. Interlaminar interface modelling for the prediction of delamination. *Composite Structures* 1992; 22: 235–242.

4. Schellekens JCJ, de Borst R. Free edge delamination in carbon-epoxy laminates: a novel numerical/experimental approach. *Composite Structures* 1994; 28: 357–373.

5. Xu XP, Needleman A. Numerical simulations of fast crack growth in brittle solids. *Journal of the Mechanics and Physics of Solids* 1994; 42: 1397–1434.

6. Ingraffea AR, Saouma V. Numerical modelling of discrete crack propagation in reinforced and plain concrete. In: Dordrecht: Martinus Nijhoff Publishers. 1985 (pp. 171–225).

7. Camacho GT, Ortiz M. Computational modelling of impact damage in brittle materials. *International Journal of Solids and Structures* 1996; 33: 2899–2938.

8. Secchi S, Simoni L, Schrefler BA. Mesh adaptation and transfer schemes for discrete fracture propagation in porous materials. *International Journal for Numerical and Analytical Methods in Geomechanics* 2007; 31: 331–345.

9. Moës N, Dolbow J, Belytschko T. A finite element method for crack growth without remeshing. *International Journal for Numerical Methods in Engineering* 1999; 46: 131–150.

10. Remmers JJC, de Borst R, Needleman A. A cohesive segments method for the simulation of crack growth. *Computational Mechanics* 2003; 31: 69–77.

11. de Borst R, Remmers JJC, Needleman A, Abellan MA. Discrete vs smeared crack models for concrete fracture: bridging the gap. *International Journal for Numerical and Analytical Methods in Geomechanics* 2004; 28: 583–607.

12. Peerlings RHJ, de Borst R, Brekelmans WAM, de Vree JHP. Gradient enhanced damage for quasi-brittle materials. *International Journal for Numerical Methods in Engineering* 1996; 39: 3391–3403.

13. Francfort GA, Marigo JJ. Revisiting brittle fracture as an energy minimization problem. *Journal of the Mechanics and Physics of Solids* 1998; 46: 1319–1342.

14. Bourdin B, Francfort GA, Marigo JJ. The variational approach to fracture. *Journal of Elasticity* 2008; 91: 5–148.

15. Miehe C, Hofacker M, Welschinger F. A phase field model for rate-independent crack propagation: Robust algorithmic implementation based on operator splits. *Computer Methods in Applied Mechanics and Engineering* 2010; 199: 2765–2778.

16. Miehe C, Welschinger F, Hofacker M. Thermodynamically consistent phase-field models of fracture: Variational principles and multi-field FE implementations. *International Journal for Numerical Methods in Engineering* 2010; 83: 1273–1311.

17. de Borst R, Verhoosel CV. Gradient damage *vs* phase-field approaches for fracture: Similarities and differences. *Computer Methods in Applied Mechanics and Engineering* 2016; 312: 78–94.

18. Dugdale DS. Yielding of steel sheets containing slits.. *Journal of the Mechanics and Physics of Solids* 1960; 8: 100–108.

19. Barenblatt GI. The mathematical theory of equilibrium cracks in brittle fracture.. *Advances in Applied Mechanics* 1962; 7: 55–129.

20. Needleman A, Tvergaard V. An analysis of ductile rupture modes at a crack tip. *Journal of the Mechanics and Physics of Solids* 1987; 35: 151–183.

21. Tvergaard V, Hutchinson JW. The relation between crack growth resistance and fracture process parameters in elastic-plastic solids. *Journal of the Mechanics and Physics of Solids* 1992; 41: 1119-1135.

22. Vignollet J, May S, de Borst R, Verhoosel CV. Phase-field models for brittle and cohesive fracture. *Meccanica* 2014; 49: 2587–2601.

23. May S, Vignollet J, de Borst R. A numerical assessment of phase-field models for brittle and cohesive fracture: Γ-convergence and stress oscillations. *European Journal of Mechanics-A/Solids* 2015; 52: 72–84.

24. Nguyen TT, Yvonnet J, Zhu QZ, Bornert M, Chateau C. A phase-field method for computational modeling of interfacial damage interacting with crack propagation in realistic microstructures obtained by microtomography. *Computer Methods in Applied Mechanics and Engineering* 2016; 312: 567–595.

25. Lee S, Wheeler MF, Wick T. Iterative coupling of flow, geomechancis and adaptive phase-field fracture including level-set crack width approaches. *Journal of Computational and Applied Mathematics* 2017; 314: 40–60.

26. Conti S, Focardi M, Iurlano F. Phase field approximation of cohesive fracture models. *Annales de l'Institut Henri Poincare (C) Non Linear Analysis* 2016; 33: 1033–1067.

27. Freddi F, Iurlano F. Numerical insight of a variational smeared approach to cohesive fracture. *Journal of the Mechanics and Physics of Solids* 2017; 98: 156–171.

28. Wu JY. A unified phase-field theory for the mechanics of damage and quasi-brittle failure. *Journal of the Mechanics and Physics of Solids* 2017; 103: 72–99.

29. Wu JY. A geometrically regularized gradient-damage model with energetic equivalence. *Computer Methods in Applied Mechanics and Engineering* 2018; 328: 612–637.

30. Geelen RJM, Liu Y, Hu T, Tupek MR, Dolbow JE. A phase-field formulation for dynamic cohesive fracture. *Computer Methods in Applied Mechanics and Engineering* 2019; 348: 680–711.

31. Wilson ZA, Landis CM. Numerical simulations of fast crack growth in brittle solids. *Journal of the Mechanics and Physics of Solids* 2016; 96: 264–290.

32. Chudwudozie C, Bourdin B, Yoshioka K. A variational phase-field model for hydraulic fracturing in porous media. *Computer Methods in Applied Mechanics and Engineering* 2019; 347: 957–982.

33. Linse T, Hennig P, Kästner M, de Borst R. A convergence study of phase-field models for brittle fracture. *Engineering Fracture Mechanics* 2017; 184: 307–318.

34. Hughes TJR, Cottrell JA, Bazilevs Y. Isogeometric analysis: CAD, finite elements, NURBS, exact geometry and mesh refinement. *Computer Methods in Applied Mechanics and Engineering* 2005; 194: 4135–4195.

35. Hageman T, de Borst R. Flow of non-Newtonian fluids in fracture porous media: Isogeometric vs standard finite element discretisation. *International Journal for Numerical and Analytical Methods in Geomechanics* 2019; 43: 2020–2037.

36. Borden MJ, Scott MA, Evans JA, Hughes TJR. Isogeometric finite element data structures based on Bézier extraction of NURBS. *International Journal for Numerical Methods in Engineering* 2011; 87: 15–47.

37. Verhoosel CV, Scott MA, de Borst R, Hughes TJR. An isogeometric approach to cohesive zone modelling. *International Journal for Numerical Methods in Engineering* 2011; 87: 336–360.

38. Chen L, Verhoosel CV, de Borst R. Discrete fracture analysis using locally refined T-splines. *International Journal for Numerical Methods in Engineering* 2018; 116: 117–140.

39. Vignollet J, May S, de Borst R. On the numerical integration of isogeometric interface elements. *International Journal for Numerical Methods in Engineering* 2015; 102: 1733–1749.